Lab on a Chip

Fabrication and Verification of a Glass-Silicon-Glass Micro-/nanofluidic Model for Investigating Multi-phase Flow in Shale-like Unconventional Dual-Porosity Tight Porous Media

Journal:	*Lab on a Chip*
Manuscript ID	LC-ART-08-2019-000847.R1
Article Type:	Paper
Date Submitted by the Author:	21-Oct-2019
Complete List of Authors:	Bai, Baojun; Missouri University of Science and Technology, Petroleum Engineering Zhang, Yandong; Missouri University of Science and Technology, Petroleum Engineering Zhou, Chuanle; Missouri University of Science and Technology, Electrical and Computer Engineering Qu, Chuang; University of Louisville, Electrical and Computer Engineering Wei, Mingzhen; Missouri University of Science and Technology, Petroleum Engineering He, Xiaoming; Missouri University of Science and Technology, Mathematics and Statistics

Fabrication and Verification of a Glass-Silicon-Glass Micro-/nanofluidic Model for Investigating Multi-phase Flow in Shale-like Unconventional Dual-Porosity Tight Porous Media

*Yandong Zhang, Chuanle Zhou, Chuang Qu, Mingzhen Wei, Xiaoming He, Baojun Bai**

Y. Zhang, Prof. M. Wei, Prof. B. Bai

Department of Geosciences and Geological and Petroleum Engineering
Missouri University of Science and Technology, Rolla, MO, 65401, USA

E-mail: baib@mst.edu

Dr. C. Zhou

Department of Electrical and Computer Engineering
Missouri University of Science and Technology, Rolla, MO, 65401, USA

Dr. C. Qu

Department of Electrical and Computer Engineering
University of Louisville, Louisville, KY, 40292, USA

Prof. X. He,
Department of Mathematics and Statistics
Missouri University of Science and Technology, Rolla, MO, 65401, USA

Keywords: microfluidics, dual-porosity, porous media, multiphase flow, direct visualization

Abstract

Unconventional shale or tight oil/gas reservoirs that have micro-/nano sizes of the dual-scale matrix pore throats with micro-fractures may result in different fluid flow mechanisms compared with conventional oil/gas reservoirs. Microfluidic model, as a potential powerful tool, has been used for decades for investigating fluid flow at pore-scale in energy field. However, almost all microfluidic models were fabricated by using etching methods and rare ones were having dual-scale micro-/nanofluidic channels. Herein, we developed a lab-based, quick-processing and cost-effective fabrication method using lift-off process combined with anodic bonding method, which opts out of using any etching methods. A dual-porosity matrix/micro-fracture pattern, which can mimic the topology of the shale with random non-regularly grain shapes was designed by Voronoi algorithm. The pore channel width range is 3 μm to 10 μm for matrices and 100-200 μm for micro-fractures. Silicon is used as the material to evaporate and deposit onto the glass wafer and then bonded with another glass wafer. The channel depth is the same 250 nm to the deposited silicon thickness. By using the advanced confocal laser scanning microscopy system (CLSM), we directly visualized the pore level flow within micro-/nano dual-scale channels with fluorescent-dyed water and oil phases. We found serious fingering phenomenon when water displacing oil in the conduits even the water has higher viscosity and the residual oil distributed as different forms in the matrices, micro-fractures and conduits. We demonstrated that different matrix/micro-fracture/macro-fracture geometries would cause different flow patterns that affect the oil recovery consequently. Taking advantage of such a micro-/nano dual-scale 'shale-like' microfluidic model fabricated by a much simpler and lower-cost method, studies on complex fluid flow behavior within the shale or other tight heterogeneous porous media would be benefited significantly.

1. Introduction

Unconventional reservoirs, including shales and other types of tight formations, which intrinsically have much lower permeability than conventional reservoirs with micro-/nano scale dual-porosity features, can exhibit highly varying properties within microscopic confinement. Therefore, microfluidic model, as a powerful pore-scale level approach is needed to better understand the flow behavior and mechanism within the heterogeneous porous media of the shale-like tight oil/gas reservois. According to the average pore-throat diameter size of unconventional shale and other tight oil/gas reservoirs, the ratio of pore surface area to the pore volume which can be 50×10^{4} cm^{-1} (approximately 700 if represented by the ratio of channel width to depth in a microfluidic model), is much larger than that of conventional porous media which can be 1.8×10^{-4} cm^{-1} (approximately 16 if represented by the ratio of channel width to depth in a microfluidic model)[1, 2]. Hence, the hypothesized surface interfacial phenomena dominated fluid flow make the liquid and gas transportation through shale are still uncertain.[3] Although some of microfluidic devices possessing dual-scale matrix/fractures network features have been built by using different fabricating method,[4-7] the channels are all in micro scale for any dimensions and not having large width-to-depth ratio (2-26), which cannot representing fluid pathways of shale or tight duel-scale reservoirs. Until recently, though the first micro-/nano PDMS-glass and quartz-glass duel-scale microfluidic models come up to represent dual scale shale, [8] the width-to-depth ratio (1-25) still stay small. Besides, the fabrication method cannot guarantees oil flow on PDMS-glass model and high-pressure experiments on glass-glass model due to the bonding issue.

Although PDMS micromodel now can realize sub-100 nm dimensions, [8, 9] it is still not a proper candidate for conducting experiments involving organic nonpolar fluids,[10] which is ubiquitous in many petroleum and environmental scenarios.[11-14] Hence, nonorganic materials based silicon-glass or glass-glass microfluidic models have risen in response and widely been

used to fabricate micro-/nanofluidic models capable of handling harsh physical and chemical conditions for energy fields.[15-19] For silicon-glass ones, since silicon has no transparency to visible light, a glass wafer is always being a transparent cover plate anodic bonded over the silicon substrate to make it possible for direct observation under a microscope.[20-22] To achieve fully transparency and for the superiorities of compatibility with many solvents,[23, 24] high stiffness for handling high pressure fluid flow experiments[25-27] and the easiness of surface wettability alteration by different methods,[28, 29] the glass itself has long been a preferred microfluidic model substrate. The choice between the two is mainly depending on the goals and needs. Silicon substrate would be chosen when one needs more precise channel sizes and straight channel side walls when using dry etching method.[30] Although glass substrates can also be dry-etched,[31, 32] the low etching rate, low etching selectivity and high facility cost make wet etching a more popular way, which make use of buffered hydrofluoric acid or mixtures of acids as the etchant solutions to etch channels on glass substrates. [33-35] The main drawback is that the isotropic wet etching process cannot reach perfect vertical walls,[33] yet this imperfect trapezoidal shape can be leveraged to generate a 2.5 D micromodel by controlling the etching depths of two neighboring pores.[36] Other fabrications of semi or fully transparent microfluidic models for energy and other fields can be found elsewhere in details.[37-42]

Among all available fabrication methods, thin film deposition, as a fast, low cost and simple process, has been used to produce micro-/nanochannels in several applications.[43-45] However, for energy field microfluidic system, it is rarely used and only as an auxiliary method to deposit a protection layer and hard mask for subsequent wet etching or dry etching process.[8, 46, 47] The aforementioned glass-quartz transparent micro-/nanofludic devices that emulates dual-scale properties of shale and tight-oil reservoirs also utilized the thin film deposition to help make the model.[8] They used thermal deposition to coat Cu film onto a lacey carbon support film and reactive ion etched the quartz substrate based on the mask. Finally, two glass wafers were bonded by continuously flushing demineralized water between the two wafers and

combining them stand for more than 3 hours.[48] However, the reactive ion etching method can produce etching byproducts that would clog the thinner channels and the 'sag' of the lacey carbon film is very likely occurred across larger apertures. Besides, it needs at least 3 to 4 days standing time for two plates bonded at least 80% strength , which is 61.8 $\pm$ 2.6 N/cm^2, to use for a fluid flow experiment. Although this bonding method can be realized at room temperature to avoid deformation of glasses at high temperature by using fusion bonding, the bonding strength and temperature resistance are questionable.

How to fabricate a 'shale-like' micro-/nanofluidic model that has a large width-to-depth ratio (12-2000) in a time-efficient and cost-effective way and meanwhile, keeping it fully transparent and strong bonding strength remains challengeable and needful these days. In this work, we, for the first time, deliver such a possibility by using the direct lift-off process combined with the anodic bonding process. For glass-based models, both wet etching and dry etching need to deposit a metal layer at first step and then do the etching at second step. The lift-off process and the etching process on a glass substrate both require the photolithography pattern and thin film deposition[49]. Therefore, instead of using any etching methods downwards the substrate, we build the grains upwards and use them directly as the intermediate layer for anodic bonding. By skipping the etching process, one may save more than 5 hours a day for fabricating 20 samples (2 cm ×2 cm) excluding other preparation times for etching. This simple, time-saving and cost-effective method improves the efficiency of fabricating a micro-/nanofluidic model significantly. The detailed fabrication processes are presented in the following sections. Finally, the functionality and practicability of the micro-/nanofluidic model are demonstrated based on the multiphase fluid flow experimental results.

2. Results and discussion

2.1. Dual-porosity Pore Network Design

To generate a complex heterogeneous porous media for investigating the multiphase flow with a microfluidic model, the Voronoi tessellation algorithm was utilized to mimic the real reservoir with random geometries and labyrinth-like pore networks.[50] The Voronoi diagram, also called Voronoi tessellation or Voronoi decomposition, is to use a computational geometry algorithm to partition a plane into different sizes of non-overlapping regions based on the closest distances among the randomly preset points on the plane[51]. However, simple Voronoi tessellation pattern with connected straight channels cannot represent the real 'convergent-divergent' conditions within the porous media and all the channels share the same width. Herein, we used the improved Voronoi tessellation algorithm in AutoCAD software to design a dual-porosity pattern with two matrices and micro-fractures connected with the matrixes with different channel widths. Further, the grains were designed as close as possible to granular shapes rather than polygonal shapes to represent the real rock grains in reservoirs, which make the pore networks have the 'convergent-divergent' profiles. As shown in Figure 1, the porous media including two matrixes and micro-fractures is sandwiched between two flow conduits, which can be regarded as macro-fractures. The lengths of two flow conduits and the porous media are 1.3 cm and 0.8 cm and the widths are 0.05 cm and 0.2 cm. Connecting to the flow conduits that have side lengths 0.1 cm are the inlet and outlet for flow injection and recovery. The outer squares with 0.3 cm side length are the pre-saturation zone to decrease the probability of blocking when injecting and recovering the fluids. The intergranular channels within the matrixes are of narrowest ones from 3 μm to 10 μm and 100-200 μm for the micro-fractures. Several vugs were also yielded by eliminating amount of grains at left and right side of the porous media. The porous media, excluding the flow conduits, consists of 192 grains with a

total porosity of 28%, which could be smaller if the vugs are not counted. The porosity for the two matrixes is approximately 5% and 23% for combined micro-fractures and vugs.

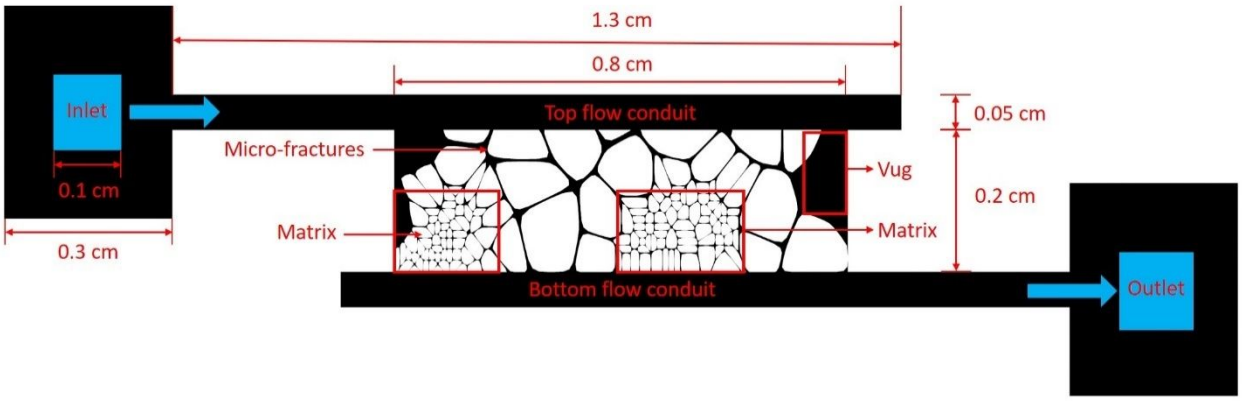

Figure 1. Dual-porosity pattern design using Voronoi algorithm

2.2. Micromodel Fabrication

The micromodel was fabricated lab-based and the successive fabrication steps of the micromodel are presented in Figure 2(a-f). A glass substrate was first spin-coated with the S1813 positive photoresist and then the pattern was developed under UV exposure followed with MF321 developer. The substrate was then loaded into a vacuum chamber and coated with an amorphous silicon layer using e-beam evaporation at an average rate of 1.6 Å/s at temperatures 16 – 50 Celsius degree . Finally, lift-off process removed the photoresist in the channels using remover-PG (a proprietary solvent stripper designed for efficient and complete removal of photoresists). The glass substrate was anodic bonded with another glass wafer after two holes were punched as inlet and outlet using UV laser. Contrast to the high cost and long fabrication workflow with wet or dry etching process for a glass-based micromodel with complex porous media patterns, this simple, fast and cost-effective fabricating method may produce amounts of micro-/nanofluidic models in a short time period (average twenty samples per day). Details of each fabrication process was discussed in the following sections.

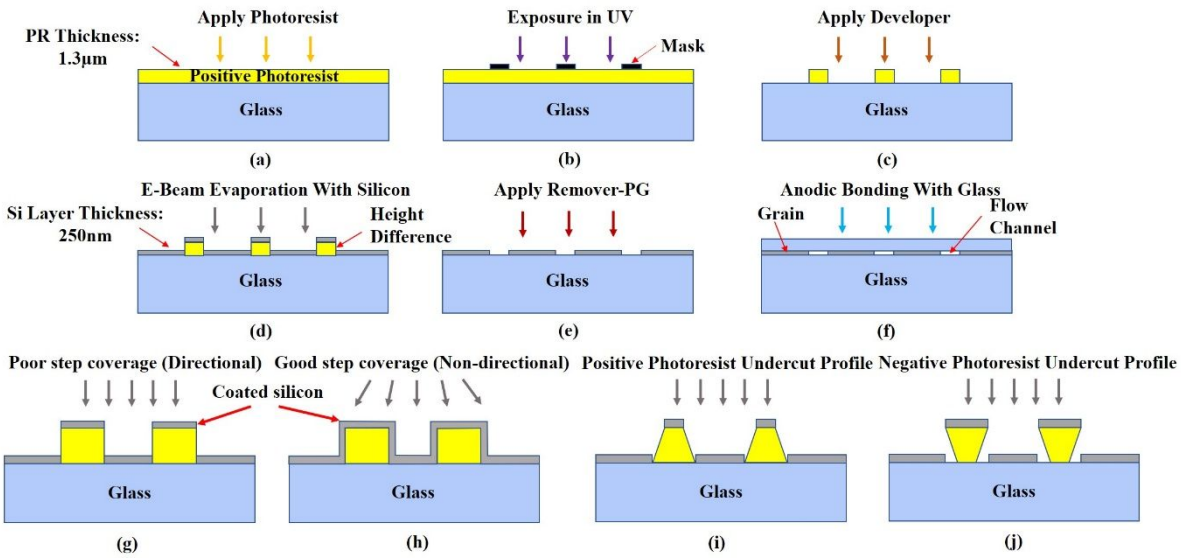

Figure 2. Schematic workflow of micro-/nanofluidic model fabrication process: (a) photoresist spin-coated on the glass substrate; (b) UV exposure to change the chemical properties of uncovered photoresist; (c) developer applied to wash away exposed photoresist; (d) e-beam evaporation used to deposit thin silicon later onto the glass substrate; (e) remover-PG used to remove residual photoresist in the channels; (f) anodic bonded with another glass wafer on top; (g)(h): illustration of deposition poor and good step coverage comparison; (i)(j): positive and negative photoresist undercut profile comparison when coated on the substrate;

2.2.1. Materials

For fabricating one complete glass-silicon-glass micromodel, two glass wafers were used as both the substrate and the cover-plate. The Schott Borofloat 33 Glass wafers are square double side polished (University Wafer), with the side length of 5 cm and the thickness of 500 ±20 µm. Silicon pellets (R.D. Mathis) were used as the evaporation material to be coated onto the glass substrate to enable an easy anodic bonding process with glass since they have the similar thermal coefficient of expansion. (For silicon is 2.6 x 10^{-6} /K and Borofloat 33 glass is 3.25 x 10^{-6}/K at 20°C).

207 ***2.2.2. Photolithography***

208 First, the glass substrate was first rinsed with acetone and methanol for two times to
209 remove dust and oil, and then blow-dried completely using dry air. The Microposit S1813
210 positive photoresist was spin coated uniformly onto the glass substrate at 4000 RPM for 40 s
211 with the thickness of 1.3 microns.Then the substrate was softbaked on the hot plate at 115
212 Celsius degrees for one minute to eliminate the moisture on the substrate. Later, the substrate
213 was soft contact with the printed polymeric mask and exposed to UV400 ultra-violet (UV) light
214 using Karl Suss MA6 aligner. The UV exposure time depends on the photo resist type. We used
215 S1813 which requires 150mJ/cm^2. The exposure power of our mask aligner is about 11mW/cm^2
216 so the exposure time is 10-15s for our samples. Lastly, the exposed photoresist was removed
217 by soaking the substrate into the MF321 developer for 50 s until the pattern can be seen clearly
218 and then rinsed using deionized (DI) water for thirty seconds. One substrate contains two
219 patterns to save the space of the substrate.

220 ***2.2.3. E-Beam Vapor Evaporation***

221 Choosing a proper evaporation method for depositing a thin silicon film on the glass
222 substrate is of great importance throughout the whole work. Different from chemical vapor
223 deposition method (CVD) that takes place at high temperatures, E-beam evaporation allows
224 depositions at relatively low substrate temperature around 16-50 Celsius degrees while yielding
225 a high deposition rate (1.6 Å/s at temperatures 16 - 50 Celsius degree) and has been used for
226 micro-electro-mechanical systems (MEMS) for a long time. [31, 52, 53] The low deposition
227 temperature prevents the deformation of the glass wafers at high temperatures around 550
228 Celsius degrees. Thermal evaporation, being as another physical evaporation, may as well heat
229 up the substrate to over 250-300 Celsius degree during deposition process.[54] Besides, chemical
230 vapor deposition may generate gaseous or liquid byproducts which may lead to impurities on
231 the substrate. Except for these two reasons in terms of deposition temperature and contaminants,
232 the most important reason for choosing e-beam physical evaporation is the consideration of the

poor step coverage of deposited film as shown in Figure 2(g) and (h). Although chemical deposition and physical sputtering both have better step coverage with isotropic deposition, this will lead to the full coverage of the surface of the substrate. The deposition would happen not only on the top of the photoresists in the channels but also the sides, which prevents the photoresist from being washed away through the open sides. On the other hand, by leveraging the directional deposition of e-beam deposition with poor step coverage, the silicon will be only deposited onto the top of the photoresist, leaving the sides open to the air. Therefore, the photoresist can be washed away easily through the open sides. To ensure the thorough removal of the photoresist, the silicon layer should be better coated less than one fourth of the photoresist layer thickness, which is 1.3 μm, to give more height difference between the photoresist layer and the silicon layer on the substrate. Thus, we chose to deposit 250 nm silicon layer. The photoresist patterned substrate was loaded in the E-beam evaporation chamber, which was pumped down to $2e^{-6}$ Torr base pressure. The E-beam deposition is at an average rate of 1.6 Å/s at temperatures 16 – 50 Celsius degree, thus it only takes no more than thirty minutes to reach ~250 nm for all loaded samples (20 per load with the sample dimension of 2 cm ×2 cm).

2.2.4. Lift-off process

The lift-off process after thin film deposition has been used for decades in semiconductor and integrated circuit (IC) areas as a simple and quick method for patterning thin metal material films. [55-57] However, it has rarely been brought into microfluidic model fabrication field. We herein utilized direct lift-off process after the E-beam evaporation process to wash away the remaining photoresists in the channels. The substrate was first soaked in the Remover-PG solution and let it stand for 10 mins. Then, the ultrasonic cleaner with deionized water was used to clear out most of the photoresist preliminarily. Later, the substrate was cleaned intensively by immersing into the Piranha Solution (3:1 H_2SO_4:H_2O_2) for 20 mins to remove the photoresist residue and other contaminants. Finally, the substrate was rinsed by deionized water and blow-dried thoroughly. The lift-off process would peel off the photoresist with top-coated silicon

259 layers from the substrate completely, leaving the channels clean to give spaces for fluid flow.
260 However, in some situations due to improper and incomplete dissolution of the photoresist, the
261 retention problem would occur. The top coated silicon would adhere to the bottom silicon grain
262 that should remain. To handle this problem, we conducted several lift-off processes with
263 deposited silicon layers of different thickness from 100 nm to 500 nm with interval of 50 nm.
264 It was not surprised that the thicker the deposited silicon layers, the more possible for rention
265 problem occurs which causes more difficultulties to wash away the photoresist. Either the side
266 windows were too small to let the remover-PG flush completely or the silicon grains were
267 peeled off together with the photoresist. The deposited material layer should not be thicker than
268 two thirds of the photoresist to ensure a complete separation.[58] However, we found that it began
269 to become difficult when the deposited silicon layer thickness is above 300 nm, which is about
270 one fourth of the photoresist thickness (1.3 μm). It is also the nature of the positive photoresist
271 that limits the height of the deposition layer. As shown in Figure 2(i) and (j), the undercut
272 profiles are different between positive and negative photoresist with the silicon deposited on
273 the top. They both have trapezoidal shapes after exposion. However, the undercut profile of
274 positive resist is less advantageous than that of the negative photoresist whose inverted one has
275 much bigger open access to the remover-PG solution. Although negative resist has been used
276 mostly in lift-off process in microelectronic field, the higher cost and the difficult removal
277 process still need to be considered. A diffuser by diverting the UV light can be utilized to change
278 the positive photoresist undercut profile to the re-entrant profile for facilitating the lift-off
279 process.[59] For our experiment, we did not use any other auxiliary method to ease the lift-off
280 process since we seriously controlled the deposited silicon layer thickness below one fourth of
281 the positive photoresist thickness to achieve a complete lift-off process.

282 ***2.2.5. Surface and Channel Characteristics***

283 After the lift-off process, the surface and the channel characteristics were analyzed. The
284 thickness of the deposited silicon was measured using Sloan Dektak 3030 surface profiler

measuring system. The probe went 300 µm across of two random grains and measured the channel depth between them. Inside the test area, the channel width is approximately 20 µm and the depth is about 277.7 nm. The surface is of good flatness, except for a few sharp peaks caused possibly by the dusts on the substrate surface. To demonstrate the profile of channel side wall, scanning electron microscopy (SEM) images of the model in tilt 45 degrees angle were taken using Hitachi S-4700 FESEM microscope as shown in Figure 3. Figure 3(a) shows the top overview of one part of the matrix and adjacent micro-fractures generated using Voronoi tessellation algorithm, which shows the matrix parts with smaller pore size while the micro-fractures with the larger pore size. Although the channel may have some degree of roughness due to the lift-off process, as shown in Figure 3(b) and (c), the channel side wall is shown to be vertical to the substrate as shown in Figure 3(d), which has better profile than wet etching.

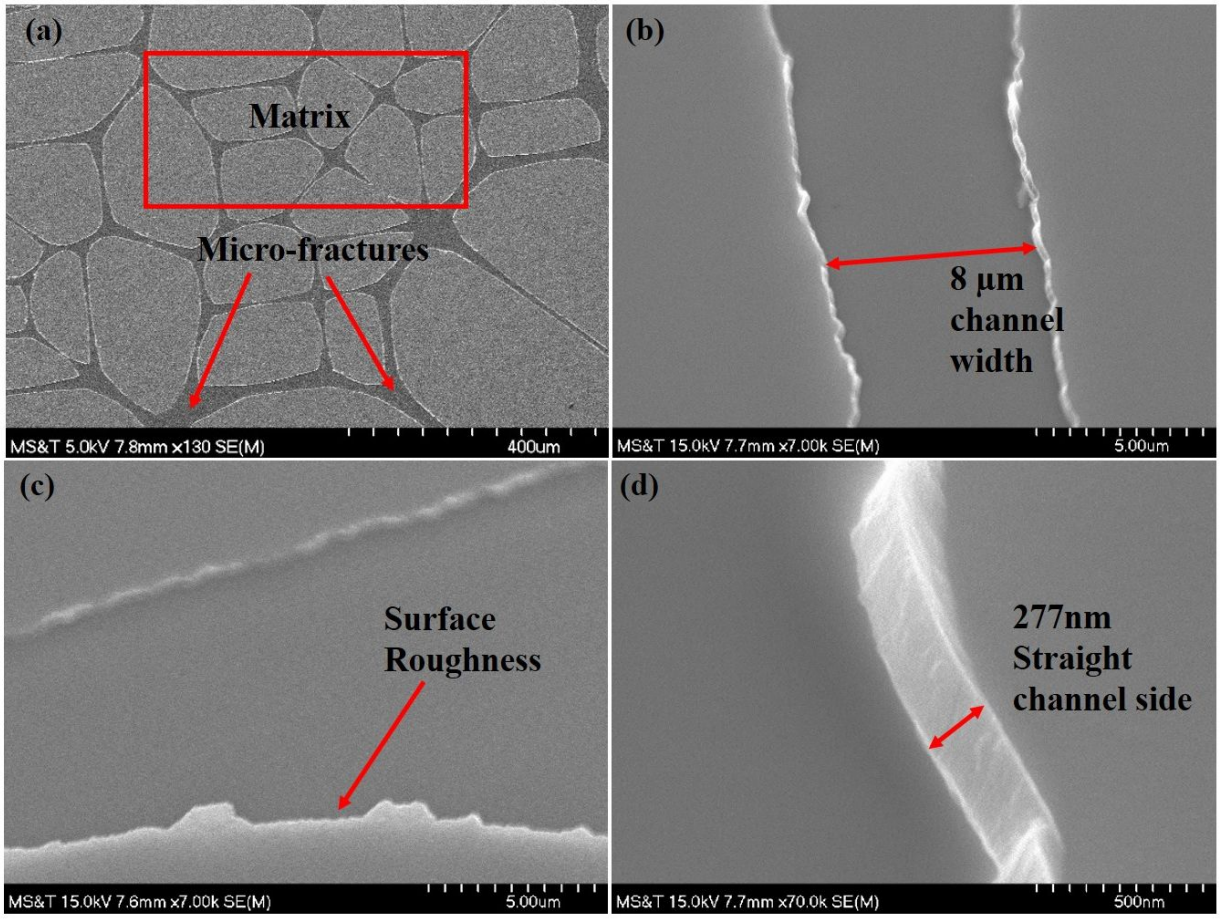

297 Figure 3. SEM images of (a) matrixes and micro-fractures demonstration; (b) matrix channel
298 with the width of 8 μm; (c) sidewall roughness; (d) straight channel wall profile with the depth
299 of 277 nm.

300 ***2.2.6. Anodic Bonding***

301 Anodic bonding can deliver strong bonding strength while keeping the substrate at low
302 temperature.[60] Glass to glass anodic bonding can be realized by using silicon or other metal
303 films as the intermediate layers and anodic bonding at no more than 400 Celsius degrees and
304 700 Volts to make it possible for optical detection with fluorescence microscopy in biological
305 and biomedical field, microfluidic systems where transparent walls were demanded.[32, 61-63] We
306 used our self-assembly anodic bonding device to conduct the final anodic bonding process to
307 seal the glass substrate with silicon layer and the plain glass cover hermetically. As shown in
308 Figure 4, Our self-assembly anodic bonding device includes a HP Keysight 6515A high voltage
309 DC power supple (0-1600V,5mA), a hot plate with an aluminum-foil paper covered, an
310 ammeter and a probe stand with a metal probe fixed. An aluminum-foil paper was wrapped
311 over the hot plate surface tightly as the conducting layer. The substrate with the silicon layer
312 was placed first onto the aluminum as layer 1, followed with the placement of the cover glass
313 onto the substrate as layer 2. Before placing, the substrate and the cover glass were already
314 rinsed together in Piranha Solution (3:1 H_2SO_4:H_2O_2) for 20 mins after lift-off process to avoid
315 bonding issue because of the residual contaminants. The SEM images also show there are not
316 visible additive residues in the channels. In the meantime, they were both changed to have
317 strong hydrophilicity. The conductive probe was adjusted vertically to press onto the cover
318 glass to initially apply a force for a pre-bond. By connecting the anode to the aluminum-foil
319 paper and cathode to the probe through the ammeter, the preparation for bonding was finished.
320 We then switched on the hotplate and set the goal temperature to around 350 Celsius degrees
321 and wait the substrate be pre-heated for 10 minutes. We used an infrared thermometer to
322 measure the surface temperature. After the temperature was stable around 350 Celsius degrees,

we slowly increased the voltage to 1200V and check the ammeter at the same time. The ammeter was being an indicator whether there is a short circuit occurred when increasing the voltage. If the current is over 1 mA at any time during voltage incensement, the voltage should decrease to zero and check the electrodes connections. The bonding process using point cathode electrode contact method can be observed, spread radially outwards from the probe pinpoint. This radial propagation process also avoids air trapping between the interface of glass and silicon. However, the bonding process cannot be completed only by contacting one point due to the large area of the chip surfaces. Therefore, whenever the spread stopped, we moved the conductive probe to another point to continue the bonding process until all parts were bonded together. This point contact bonding method is much faster than the flat cathode electrode contact method and also costless.[64] It is also noteworthy that there were no collapsed channels found after the anodic bonding process. The channel aspect ratio (depth to width) has been demonstrated to be a crucial diameter when conducting a bonding process for either glass-silicon or glass-glass models.[65] For a glass cover anodic bonded onto a silicon substrate, due to the applied strong electrical force, the top and bottom surfaces would contact and seal the channel permanently if the aspect ratio is smaller than 0.004. For a fusion bonding process between two glass wafers, the high temperature would deform the glass material and thus cause the collapse of the channels if the aspect ratio is smaller than 0.0005. For our anodic bonding process under low temperature, there are also no strong electrical interactions between the top and bottom glass wafers. Therefore, the channels were all survived with the aspect ratio even smaller than 0.0005.(e.g. conduits and the vugs).

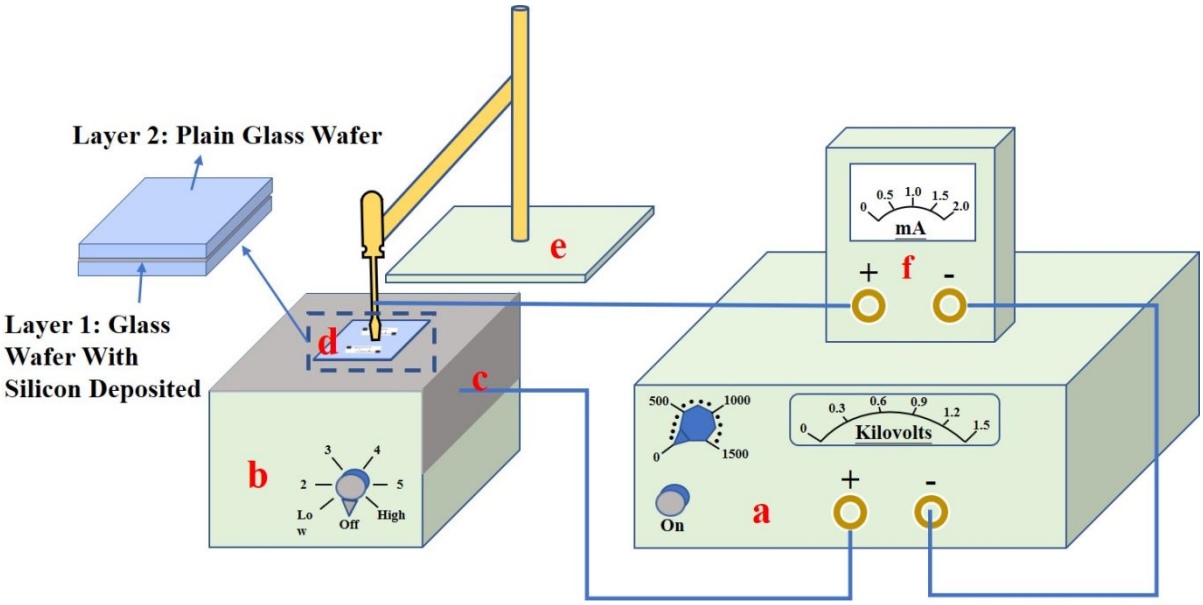

Figure 4. Schematic of the lab-based anodic bonding apparatus. a. high voltage DC power supple (0-1600V,5mA); b. hot plate; c. aluminum paper; d. two glass wafers with an intermediate silicon layer; e. probe stand; f. amperemeter;

3. Experimental verification for the glass-silicon micromodel

We tested the practicability of the glass-silicon-glass micromodel by conducting a two-phase fluid displacement experiment. Deionized water (DI water) was used as the wetting phase and decane as the non-wetting phase. The fluid flow process was investigated by utilizing confocal laser scanning microscopy (CLSM). To distinguish the two kinds of fluids under different lasers, they were both fluorescent-dyed using Alexa Flour 594 for the water phase and Nile Red for the oil phase (both from Sigma-Aldrich), respectively. The DI water was in red and the decane was in green after separately excited by lasers at 488 nm and 561 nm. The micromodel was firstly saturated with the decane injected by using syringe pump (Harvard Apparatus, model 88-3015). Then the decane was displaced by the DI water at the flow rate of 0.02 mL/hr. Because it is a large field micromodel, even if we used 10 X objective lens that have the biggest vision of field among all lenses, we can only observe partial areas. Therefore, the stage was set moved automatically from left corner inlet to the right corner outlet with 19 horizontal steps and 5 vertical steps. All fields were then stitched together to obtain a whole

image which covers all parts of the model. We scanned and recorded the whole injecting process using resonant scanning mirrors instead of traditional galvanometer mirrors to acquire high scanning speed. Although the resolution became worse, the scanning speed can be up to 7.7 frame per second and it takes only 40 seconds to scan the whole model. All experiments were conducted at room temperature.

3.1. Oil Saturation Process

In this research, since our focus is to fabricate the model and verify its usability to conduct a flooding experiment, we did not consider the irreducible water saturation to mimic the real reservoir saturation history as it is neglectable for verifying the usability of this model. Therefore, we only did the water flooding imbibition test by directly saturating the model with oil first. Decane (0.92 cP at 20°C) was injected using 1/16-inch inner diameter tubing into the inlet nanoport (IDEX Health & Science LLC) at flow rate of 0.02mL/L. As shown in Figure 5, it took about 10 hours to fully saturate the microfluidic model with decane phase. The flow direction was from top left corner inlet to the bottom right outlet where was always open to the air with no backpressure added. From the time sequence from top to the bottom with the time interval of 2 hours, we can observe that the intensity of fluorescent was increased with the gradually saturation of the oil phase. From T =4 hrs, the flow started to flow into the bottom conduit, mostly from the middle micro-fractures other than the matrix at left, which verifies the assumption for the interface conditions in to govern the coupled flow in a dual-porosity media and its adjacent conduits[66]. At T = 6 hrs, the bottom conduit has more fluid flown into than the matrix at right. Until the end of the injection, except for the left corner of the bottom conduit, all the top and bottom conduits were saturated, together with the two matrixes and micro-fractures. The bonding failure may occur at the edges of the inlet and outlet, as well as some edges at the matrix boundaries as indicated in Figure 5 (T= 10 hrs). The partial bonding failure would not affect the general trend of the fluid flow inside the porous media seriously. We did

not observe any leakage from the chip until the injecting pressure was higher than 420 Psi when the solidified epoxy that fixed the nanoport on the chip started to crack and leak but not for other parts of the model. However, our injecting pressure was no more than 200 Psi so there was no leakage observed throughout the experiments.The water phase was then ready to be injected until there was no fluorescent intensity increase observed which means the porous media was fully saturated with the decane oil phase.

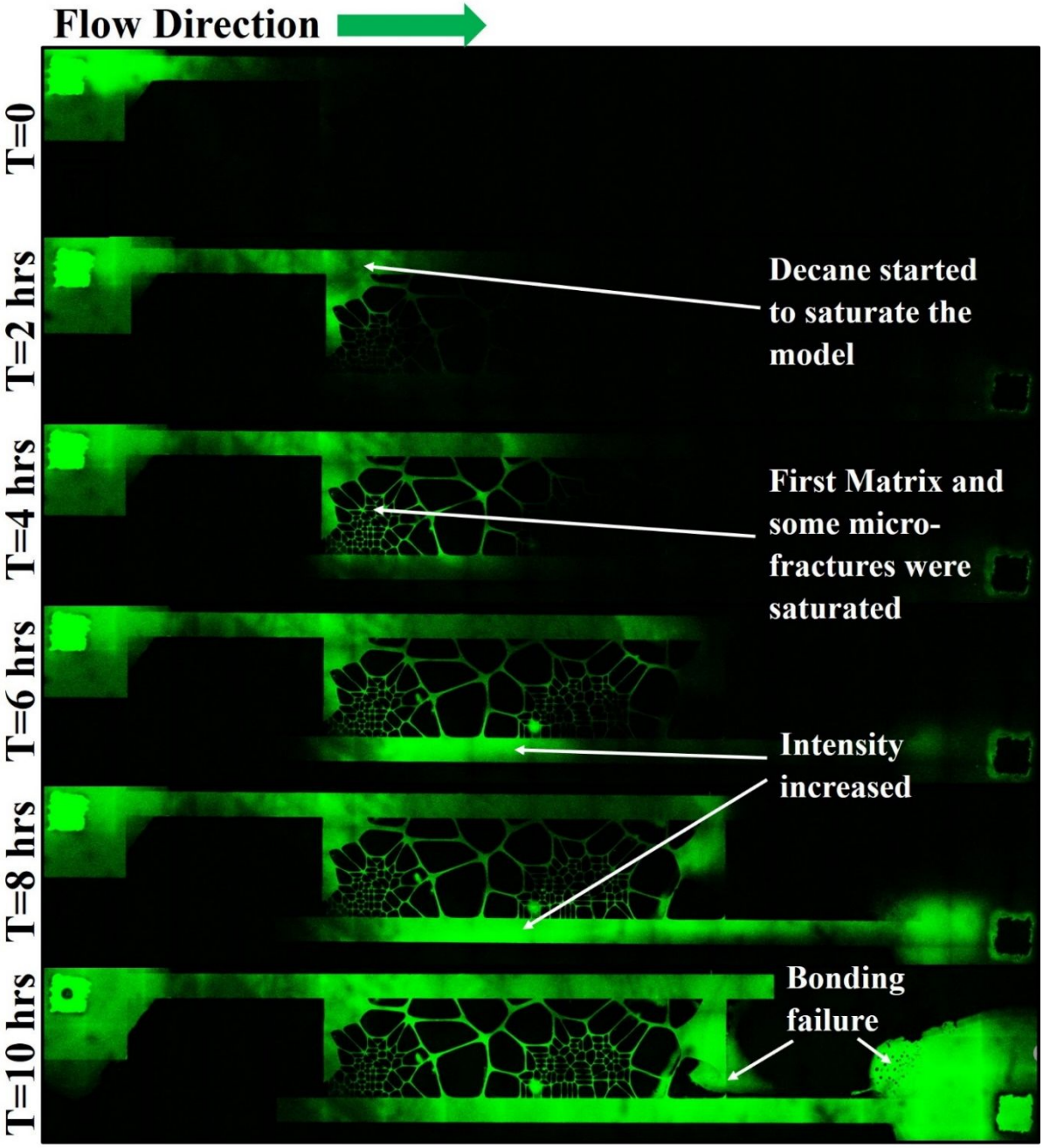

Figure 5. Oil saturation process in a time sequence (top to bottom) with flow direction (left to right).

3.2. Forced water imbibition process

We conducted the water imbibition processes in two directions with constant flow rate of 0.02mL/hr. One is positive injection from the inlet, another one is reverse injection from the outlet. The two matrixes were adjacent to the bottom conduit when the water was forwardly injected into the micromodel, while adjacent to the top conduit when the water was reversely injected. The decane oil phase and water phase were in true excitation color of green and red. Both two imbibition processes were successful with no leakage found and stopped at about fifty minutes when no more significant phase changes after water breakthrough within the models.

Because of the strong hydrophilicity of glass and silicon layer after rinsed in piranha solution before bonding, and with the very low flow rate, the water intended to be imbibed into the matrixes first other than micro-fractures from top conduit. For the forward injection process as shown in Figure 6, the water started to invade into the top conduit and imbibed into the first matrix at the same time at around 5 minutes from the imbibition beginning. The waterflow then branched into two different directions. One branch continued to flow in the conduit and another branch flew into the bottom conduit. Although some of the water in the matrix flew into the middle micro-fractures, quicker flow velocity was found at top and bottom conduits. Consequently, at T=8 minutes, the water from the top conduit was imbibed into the second matrix and started to displace the oil into the bottom conduit forced by the backpressure of water behind it. Since the decane oil is less viscous than the water, a fingering phenomenon was observed as the oil flow had a finger-like structure as it travelled towards the outlet while remained connected. Besides, as the pressure built up within the whole model, part of the remaining oil at upstream conduit was also started to be displaced and also acted finger-like when it met the water that has already been in the top conduit as shown at T=10 and 15 minutes.

The fingering became more remarkable at T=30 minutes at both conduits and some of the matrixes and micro-fractures were re-saturated by some upstream remaining oil. From T=30 minutes to T=50 minutes, there were no other significant changes, but some connected finger-like oil was stretched longer or disconnected into dispersed oil droplets by the continuously water flooding. The fingering phenomenon was also found in the reverse injection process. However, it happened mostly only in the bottom conduit while only rare were found in the top conduit as shown in Figure 7. At the beginning, the water flew uniformly into the top conduit with much less remaining oil left at upstream conduit. The water reached the first matrix on the top at T=6 to T=8 minutes and imbibed into it. Meanwhile, some water was also diverted towards the left-side vug. At T=9 minutes, the water in the first matrix started to flow into the bottom conduit and continued to flow right to the middle micro-fractures afterwards. As the water in the top conduit insisted to reach the second matrix at the top right corner, the water in the micro-fractures firstly flew into the bottom conduit and converge with water from the second matrix later at T=10 minutes. The fingering occurred in the bottom conduit at T=15 minutes as the upstream remaining oil in the bottom conduit was displaced towards the outlet and became the most serious at T=50 minutes. Although there was also some fingering observed at the boundaries of the top conduit, it was much less significant than that of the scenario in which the water was forwardly injected. The hypothesized reason is that, when the water was forwardly injected, the two matrixes were much closer to the inlet, which may generate a strong imbibition area for the water at the very beginning of the flooding process. On the contrast, the two matrixes were adjacent to the top conduit and farther to the inlet. Therefore, the water would not prefer to flow into the micro-fracture at the beginning, but rather to flow steadily in the top conduit until reached the first matrix. Thus, there were much less remaining oil left at the upstream since most of them were already been displaced through the top conduit. As a result, the fingering was not likely to be found in the top conduit for the reverse injection scenario, which in return leads to a higher oil recovery.

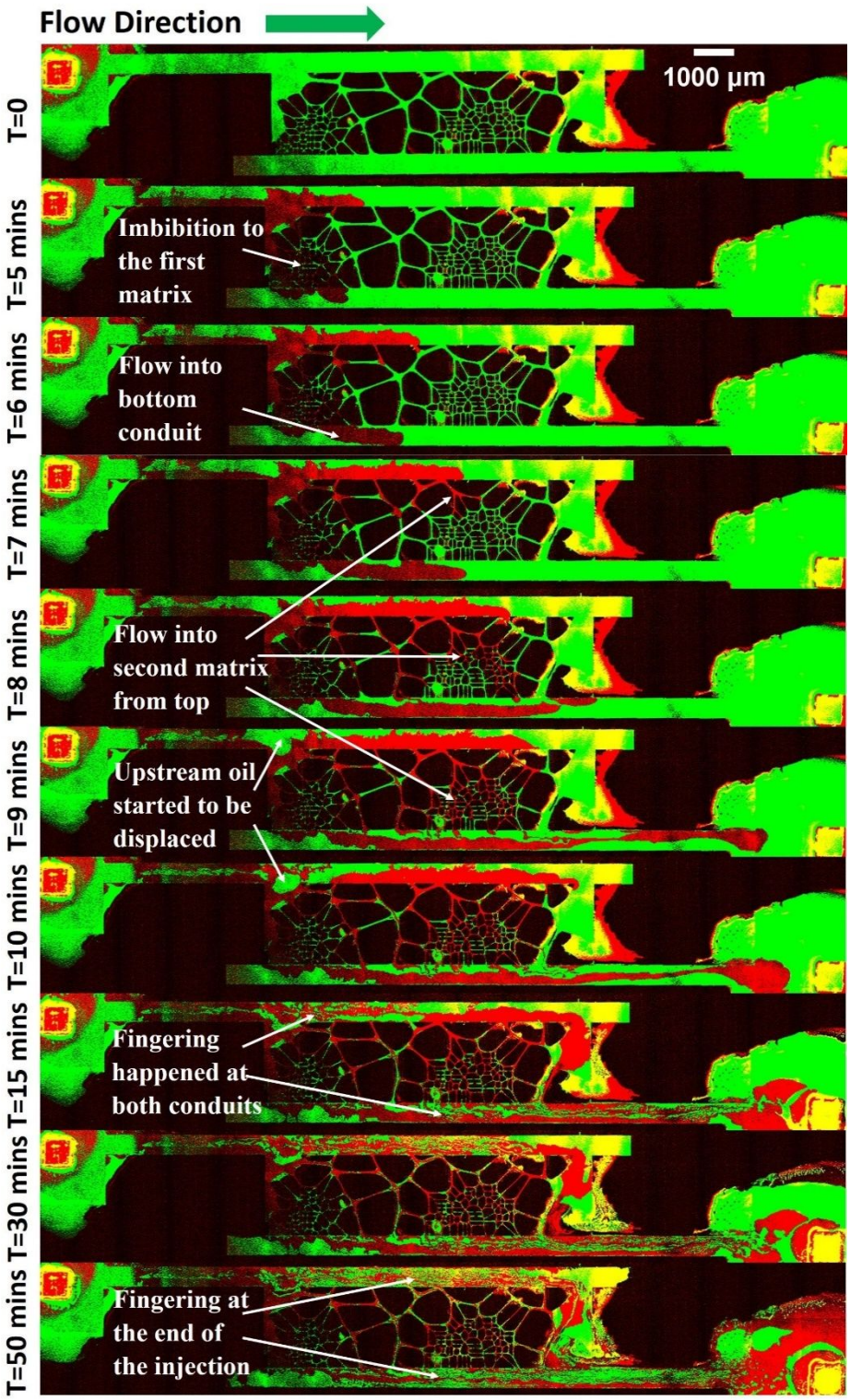

Figure 6. Water imbibition process in a time sequence (top to bottom) with flow direction (left to right).

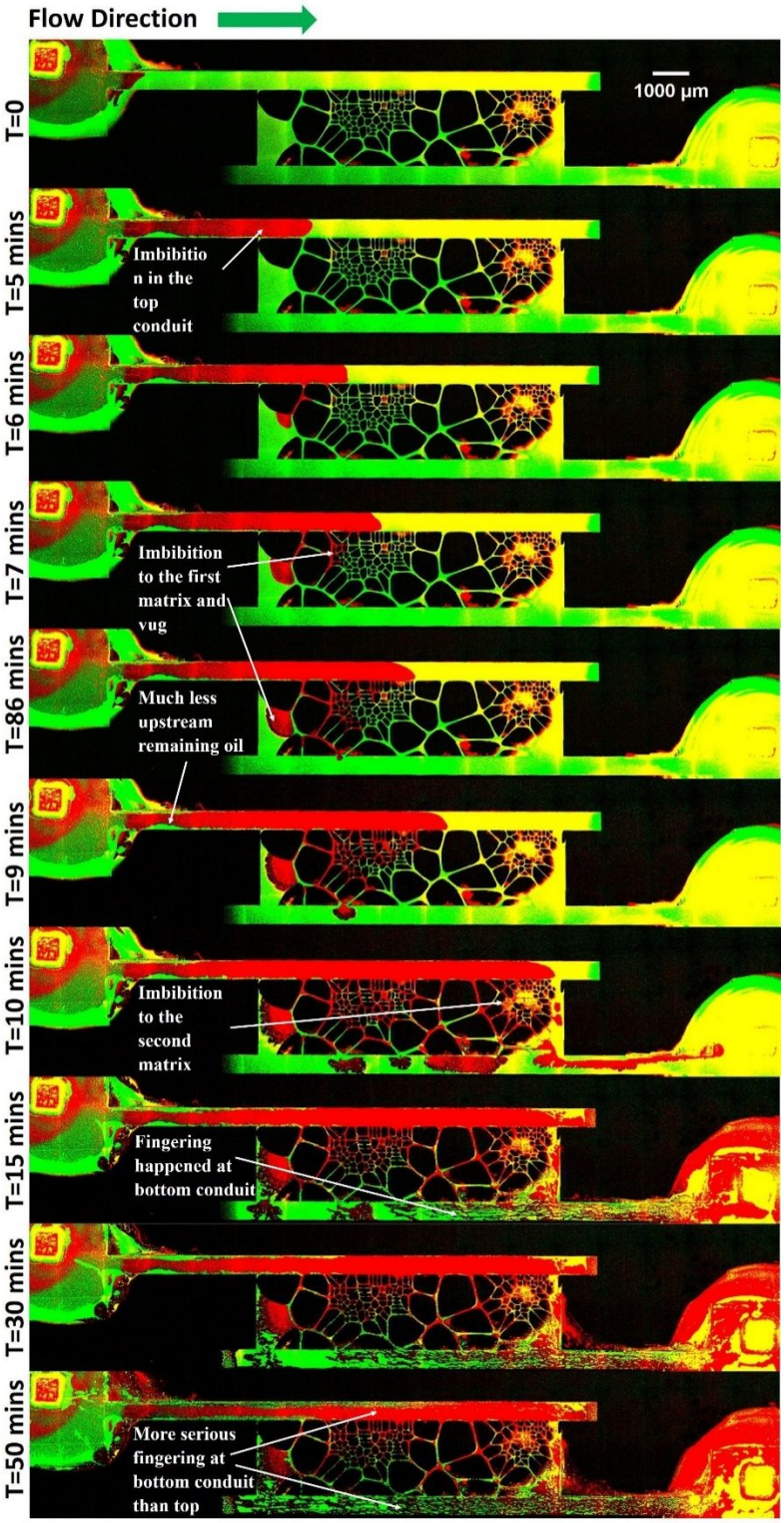

Figure 7. Reverse water imbibition process in a time sequence (top to bottom) with flow direction (left to right).

3.3. Residual oil distribution comparison

The residual oil is the oil that cannot be recovered by simple conventional water flooding method. We repeated the experiments in other two models built with the same method and still found the residual oil was much less when the two matrixes were adjacent to the top conduit than that of the case in which the two matrixes were adjacent to the bottom conduit. For both cases, the residual oil would exist in different forms within the matrixes as shown in Figure 8(a) and (b) and the microfractures as shown in Figure 8(c) and (d). Some of them were adhered to the rough surface and cannot be displaced by the water while most of them left in the middle of the channel in different shapes. Besides, snap-off was also observed at very thin matrix channel, resulting in slugs of oil droplet trapped in the pore throat with water phase filled among them. It was also found that the re-saturated oil can be hardly driven by following water flooding process when the two matrixes were adjacent to the bottom conduit, which causes much more residual oil as shown in Figure 8(b) and (d) than that of reverse injection case as shown in Figure 8(a) and (c). However, the residual oil distributed similarly in the bottom conduit for both cases, as the finger-structured oil plumes were destroyed by constantly water flooding and randomly dispersed with the direction pointing to the outlet.

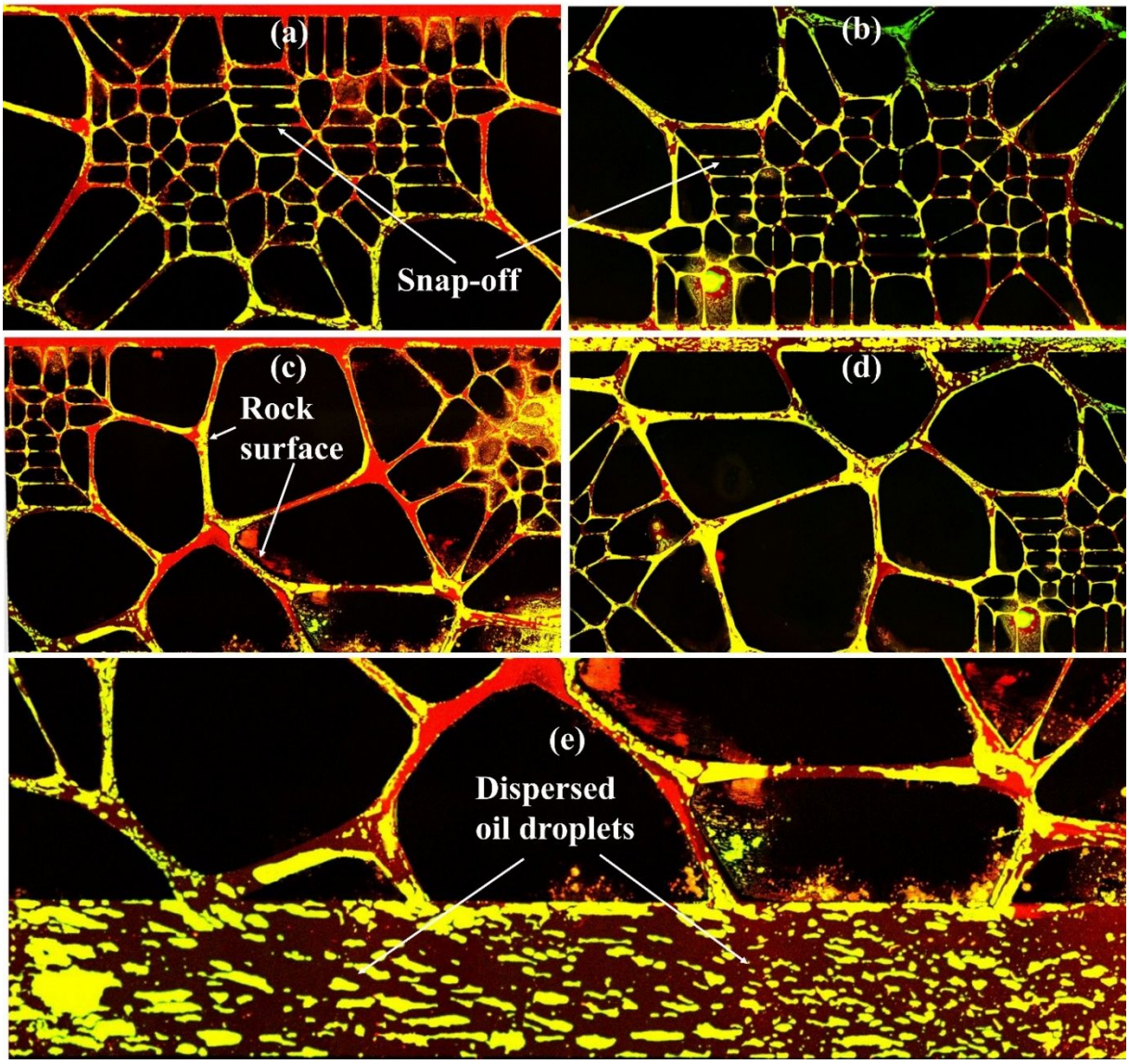

Figure 8. Residual oil distribution conditions comparisons in matrixes, micro-fractures of two different geometries (a) and (c) top conduit with adjacent matrixes; (b) and (d) bottom conduit with adjacent matrixes; (e) bottom conduit.

3. Conclusion and future work

We successfully used e-beam physical evaporation deposition, lift-off process and anodic bonding method to fabricate a fully transparent, shale-like dual-porosity glass-silicon-glass micro-nonofluidic model in a simple, fast and low-cost way. The fabrication process gets rid of the time-consuming and complicated etching method while still generates complex porous media network with uniform channels in a much shorter time. To verify the functionally and practicability of the model, two phase fluid flow displacement experiments with two injection modes were conducted separately and visualized using confocal laser scanning microscope. Owing to the large width-to-depth ratio range (12-2000) of the model, especially for two conduits at top and bottom, the fingering phenomena that may happen in a Hele-Shaw cell were brought into sight. Moreover, we observed that it is possible the fingering problem could exist when displacing phase viscosity is higher than that of the displaced phase due to the geometry of the porous media. Besides, the residual oil distributed as different forms in the matrixes, micro-fractures and conduits. Snap-offed oil droplets trapped in thin channel pore throat, oil chains left in the wider matrix channels, boundary-adhered oil films due to the surface roughness, and the dispersed oil droplets in the conduits were found, respectively. By changing the flow pattern by shifting two matrixes adjacent to the bottom and then top conduits, we demonstrated that different matrix/micro-fracture/macro-fracture interlacing geometries that may affect flow patterns, which would affect the oil recovery seriously for dual-porosity heterogeneous shale porous media.

Although this micro-/nanofluidic model provides with a quick and simple platform for direct visualizing the fluid flow dynamically in a dual-scale porous media, there are still further expectations for the future work. The micro-/nanofludic model can be improved by designing more different patterns that representing more complicated reservoir conditions. The limitation of depth-to-width aspect ratio by using glass-glass anodic bonding method still needs further

investigated, which would provide the possibility of fabricating the micromodel even at sub-10 nm scale. The residual oil distribution, flow velocity, pressure difference and fingering problem are still need further researched quantitatively and systematically to get a comprehensive understanding of the fluid flow within dual-scale micro-/nano channels at pore level.

Author contributions

Y. Zhang designed and fabricated the microfluidic chips, implemented experiments, and prepared the original manuscript. C. Zhou offered the use of photolithography equipment and materials, gave guidance and suggestions to lift-off process. C. Qu offered the use of the E-beam evaporator and deposition materials, gave guidance and suggestions to E-beam evaporation deposition process. B.Bai is the principle supervisor and advisor of this research. M. Wei and X. He are the co-supervisors and co-advisors of this research. All superviors proposed the conceptualization of this research and provided the funding support. All authors had discussions with the results and contributed to manuscript correction and proofread.

Conflict of Interest

The authors declare no conflict of interest.

Acknowledgement

This research was supported by National Science Foundation grants 1722647.

References

1. A. Boruah, A. Rasheed, V. A. Mendhe and S. Ganapathi, *Journal of Petroleum Exploration and Production Technology*, 2019, **9**, 1041-1050.
2. P. H. Nelson, *AAPG bulletin*, 2009, **93**, 329-340.
3. F. Civan, C. S. Rai and C. H. Sondergeld, *Transport in porous media*, 2011, **86**, 925-944.
4. K. Xu, P. Zhu, T. Colon, C. Huh and M. Balhoff, *SPE Journal*, 2017, **22**, 459-469.
5. C. A. Conn, K. Ma, G. J. Hirasaki and S. L. Biswal, *Lab on a Chip*, 2014, **14**, 3968-3977.
6. W. Yun, C. M. Ross, S. Roman and A. R. Kovscek, *Lab on a Chip*, 2017, **17**, 1462-1474.

7. M. Buchgraber, M. Al-Dossary, C. Ross and A. R. Kovscek, *Journal of Petroleum Science and Engineering*, 2012, **86**, 27-38.
8. S. A. Kelly, C. Torres-Verdín and M. T. Balhoff, *Lab on a Chip*, 2016, **16**, 2829-2839.
9. R. Peng and D. Li, *Lab on a Chip*, 2016, **16**, 3767-3776.
10. J. N. Lee, C. Park and G. M. Whitesides, *Analytical chemistry*, 2003, **75**, 6544-6554.
11. R. F. Herrick, M. D. McClean, J. D. Meeker, L. K. Baxter and G. A. Weymouth, *Environmental Health Perspectives*, 2004, **112**, 1051-1053.
12. G. Weaver, *Environmental science & technology*, 1984, **18**, 22A-27A.
13. J. Geng, H. Ding, P. Han, Y. Wu and B. Bai, *Energy & fuels*, 2018, **32**, 8358-8365.
14. J. Geng, J. Pu, L. Wang and B. Bai, *Fuel*, 2018, **223**, 140-148.
15. E. Parsa, X. Yin and E. Ozkan, *SPE Annual Technical Conference and Exhibition*. Society of Petroleum Engineers, 2015.
16. N. S. K. Gunda, B. Bera, N. K. Karadimitriou, S. K. Mitra and S. M. Hassanizadeh, *Lab on a Chip*, 2011, **11**, 3785-3792.
17. M. Alfi, H. Nasrabadi and D. Banerjee, *Fluid Phase Equilibria*, 2016, **423**, 25-33.
18. Y. Lin, X. Yu, Z. Wang, S.-T. Tu and Z. Wang, *Analytica chimica acta*, 2010, **667**, 103-112.
19. S. G. Lefortier, P. J. Hamersma, A. Bardow and M. T. Kreutzer, *Lab on a Chip*, 2012, **12**, 3387-3391.
20. Q. Wu, J. T. Ok, Y. Sun, S. Retterer, K. B. Neeves, X. Yin, B. Bai and Y. Ma, *Lab on a Chip*, 2013, **13**, 1165-1171.
21. Q. Wu, B. Bai, Y. Ma, J. T. Ok, X. Yin and K. Neeves, *Spe Journal*, 2014, **19**, 793-802.
22. J. W. Grate, R. T. Kelly, J. Suter and N. C. Anheier, *Lab on a Chip*, 2012, **12**, 4796-4801.
23. K. Ren, J. Zhou and H. Wu, *Accounts of chemical research*, 2013, **46**, 2396-2406.
24. H. Doryani, M. Malayeri and M. Riazi, *Fuel*, 2016, **182**, 613-622.
25. F. Kazemifar, G. Blois, D. C. Kyritsis and K. T. Christensen, *Water Resources Research*, 2015, **51**, 3017-3029.
26. M. Sohrabi, D. Tehrani, A. Danesh and G. Henderson, *SPE Annual Technical Conference and Exhibition*. Society of Petroleum Engineers, 2001.
27. R. Bora, B. Maini and A. Chakma, *SPE Reservoir Evaluation & Engineering*, 2000, **3**, 224-229.
28. J. W. Grate, M. G. Warner, J. W. Pittman, K. J. Dehoff, T. W. Wietsma, C. Zhang and M. Oostrom, *Water Resources Research*, 2013, **49**, 4724-4729.
29. A. Maghzi, S. Mohammadi, M. H. Ghazanfari, R. Kharrat and M. Masihi, *Experimental Thermal and Fluid Science*, 2012, **40**, 168-176.
30. K. Kawai, F. Yamaguchi, A. Nakahara and S. Shoji, *Proc. 14th Int. Conf. Miniaturized Syst. Chem. Life Sci.(MicroTAS)* , 2010, 1193-1195.
31. M. Bu, T. Melvin, G. J. Ensell, J. S. Wilkinson and A. G. Evans, *Sensors and Actuators A: Physical*, 2004, **115**, 476-482.
32. V. Kutchoukov, F. Laugere, W. van Der Vlist, L. Pakula, Y. Garini and A. Bossche, *Sensors and Actuators A: Physical*, 2004, **114**, 521-527.
33. M. Castano-Alvarez, D. F. P. Ayuso, M. G. Granda, M. T. Fernández-Abedul, J. R. García and A. Costa-García, *Sensors and Actuators B: Chemical*, 2008, **130**, 436-448.
34. C. Iliescu, B. Chen and J. Miao, *Sensors and actuators A: Physical*, 2008, **143**, 154-161.
35. J. Wan, T. K. Tokunaga, C. F. Tsang and G. S. Bodvarsson, *Water resources research*, 1996, **32**, 1955-1964.
36. K. Xu, T. Liang, P. Zhu, P. Qi, J. Lu, C. Huh and M. Balhoff, *Lab on a Chip*, 2017, **17**, 640-646.
37. X. Chen and L. Zhang, *Sensors and Actuators B: Chemical*, 2018, **254**, 648-659.
38. A. Anbari, H. T. Chien, S. S. Datta, W. Deng, D. A. Weitz and J. Fan, *Small*, 2018, **14**, 1703575.
39. M. L. Kovarik and S. C. Jacobson, *The Journal of Physical Chemistry B*, 2009, **113**(49), 15960-15966.
40. C. Iliescu, H. Taylor, M. Avram, J. Miao and S. Franssila, *Biomicrofluidics*, 2012, **6**, 016505.
41. V. A. Lifton, *Lab on a Chip*, 2016, **16**, 1777-1796.
42. N. Karadimitriou and S. Hassanizadeh, *Vadose Zone Journal*, 2012, **11**.
43. P. Mao and J. Han, *Lab on a Chip*, 2009, **9**, 586-591.

44. F. Liang, A. Ju, Y. Qiao, J. Guo, H. Feng, J. Li, N. Lu, J. Tu and Z. Lu, *Lab on a Chip*, 2016, **16**, 984-991.
45. Y. Kanno, K. Ino, H. Shiku and T. Matsue, *Lab on a Chip*, 2015, **15**, 4404-4414.
46. D. Bien, P. Rainey, S. Mitchell and H. Gamble, *Journal of Micromechanics and Microengineering*, 2003, **13**, S34.
47. R. Müller, P. Schmid, A. Munding, R. Gronmaier and E. Kohn, *Diamond and related materials*, 2004, **13**, 780-784.
48. Z.-J. Jia, Q. Fang and Z.-L. Fang, *Analytical chemistry*, 2004, **76**, 5597-5602.
49. J. Park, N.-E. Lee, J. Lee, J. Park and H. Park, *Microelectronic engineering*, 2005, **82**, 119-128.
50. M. Wu, F. Xiao, R. M. Johnson-Paben, S. T. Retterer, X. Yin and K. B. Neeves, *Lab on a Chip*, 2012, **12**, 253-261.
51. A. Okabe, B. Boots, K. Sugihara and S. N. Chiu, *Spatial tessellations: concepts and applications of Voronoi diagrams*, John Wiley & Sons, 2009.
52. J. Kim, Z. Li and I. Park, *Lab on a Chip*, 2011, **11**, 1946-1951.
53. A. Han, O. Wang, M. Graff, S. K. Mohanty, T. L. Edwards, K.-H. Han and A. B. Frazier, *Lab on a Chip*, 2003, **3**, 150-157.
54. A. Piegari and F. Flory, *Optical thin films and coatings: From materials to applications*, Woodhead Publishing, 2018.
55. D. W. Widmann, *IEEE Journal of Solid-State Circuits*, 1976, **11**, 466-471.
56. S. Weichel, R. De Reus and M. Lindahl, *Sensors and Actuators A: Physical*, 1998, **70**, 179-184.
57. Y.-J. Chen, J.-H. Hsu and H.-N. Lin, *Nanotechnology*, 2005, **16**, 1112.
58. H. I. Smith, *Proceedings of the IEEE*, 1974, **62**, 1361-1387.
59. H. S. Lee and J.-B. Yoon, *Journal of Micromechanics and Microengineering*, 2005, **15**, 2136.
60. K. Knowles and A. Van Helvoort, *International materials reviews*, 2006, **51**, 273-311.
61. A. Berthold, L. Nicola, P. Sarro and M. Vellekoop, *Sensors and Actuators A: Physical*, 2000, **82**, 224-228.
62. P. Knapkiewicz, B. Cichy, W. Posadowski, K. Tadaszak, P. Sniadek and J. Dziuban, *Procedia Engineering*, 2011, **25**, 1629-1632.
63. J. Kameoka and H. Craighead, *Sensors and Actuators B: Chemical*, 2001, **77**, 632-637.
64. C. Tripathi, S. Jain, P. Joshi, S. Sood and D. Kumar, *Indian Journal of Pure & Applied Physics*, 2008, **46**, 738-743.
65. P. Mao and J. Han, *Lab on a Chip*, 2005, **5**, 837-844.
66. J. Hou, M. Qiu, X. He, C. Guo, M. Wei and B. Bai, *SIAM Journal on Scientific Computing*, 2016, **38**, B710-B739.

Fabrication and Verification of a Glass-Silicon-Glass Micro-/nanofluidic Model for Investigating Multi-phase Flow in Shale-like Unconventional Dual-Porosity Tight Porous Media

*Yandong Zhang, Chuanle Zhou, Chuang Qu, Mingzhen Wei, Xiaoming He, Baojun Bai**

Time efficient and costless lift-off process combined with anodic bonding method was used to create a 'shale-like' glass-silicon-glass microfluidic model.